Journal of Energy Storage 70 (2023) 108056

Contents lists available at ScienceDirect

Journal of Energy Storage

journal homepage: www.elsevier.com/locate/est

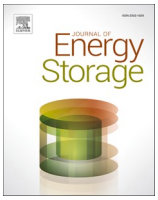

Research papers

An electrode for a high-performance asymmetric supercapacitor made of rGO/PANI/PB ternary nanocomposite

H.M. Mohamed [a], M.M. Abo-Aly [a], S.M. Abdel Wahab [a], M.A. Mousa [b], Asmaa A.I. Ali [b,*]

[a] Chemistry Department, Faculty of Science, Ain-Shams University, Cairo, Egypt
[b] Chemistry Department, Faculty of Science, Benha University, Benha, Egypt

ARTICLE INFO

Keywords:
Supercapacitor
Prussian blue
Nanocomposite
Electrochemical
Specific capacitance

ABSTRACT

The electrodeposition technique was used to create Prussian blue (PB), binary: rGO/PB, PANI/PB, rGO/PANI, and ternary: rGO/PANI/PB nanocomposites. X-ray diffraction (XRD), Fourier transform infrared spectroscopy (FT-IR), scanning electron microscope (SEM), and Brunauer–Emmett–Teller (BET) methods were used to describe the samples. The results demonstrated the covering of PB by the rGO and PANI. The electrochemical characteristics of the studied materials were examined using cyclic voltammetry (CV), galvanostatic charge and discharge (GCD), and electrochemical impedance spectroscopy (EIS) in 2 M Na_2SO_4. The specific capacitance follows the order: rGO/PANI/PB > rGO/PB > PANI/PB > rGO/PANI> PANI > rGO > PB. The rGO/PANI/PB nanocomposite electrode exhibits a specific capacitance of 336 F. g^{-1} in 2 M Na_2SO_4 at a discharge current density of 1 A. g^{-1} with 92 % retention of its original capacitance after 3000 cycles. The remarkable electrochemical performance of the ternary rGO/PANI/PB nanocomposite is attributed to its synergistic effects among individual components. The ternary electrode's high electrochemical performance indicates that it might be employed as an electrode for commercial supercapacitors. An asymmetric supercapacitor (ASC) was built using a positive electrode of rGO/PANI/PB and a negative electrode of activated carbon (AC). The arranged (ASC) operates continuously within the potential range of 0–1.8 V and delivers a high energy density of 56.3 Wh. kg^{-1} at a power density of 8804 W. kg^{-1}, as well as 92 % retention of its original capacitance after 3000 cycles.

1. Introduction

Due to the depletion of fossil fuel stocks, and the escalating environmental issues, there is a significant need for a renewable, environmentally friendly energy conversion and storage technology, which involves batteries, fuel cells, capacitors, and supercapacitors [1–3]. Among various energy storage devices, supercapacitor technology has attracted significant attention for high-power applications because of its higher power density, fast charging-discharging rate, wide working temperature range, and long cycling life [4,5].

Depending on how they store energy, supercapacitors are divided into the following categories: the electric double layer capacitor (EDLC), of which capacitance results from charge storage electrostatically at the interfaces between the electrodes and electrolyte solution, and pseudocapacitors electrodes such as metal oxides materials with different oxidation states and conducting polymers, which create charge storage due to the fast reversible redox (faradaic) process. Based on combining the benefits of double-layer capacitance and pseudocapacitance, hybrid capacitors with distinguished super capacitance and high stability have recently been developed [6–10].

Prussian blue (PB) is a mixed-valence iron cyanide complex with a general formula of $Fe_4[Fe(CN)_6]_3.xH_2O$. It exhibits a cubic array with six cyano groups attached to each Fe ion and edges composed of Fe^{2+}-CN-Fe^{3+} chains, which correspond to cubic face-centered unit cells [11]. PB exhibits two important properties (i) large three-dimensional diffusion channels causing a weak contact with any diffusing ion improving ion transport both inward and outward (ii) the presence of two independent of $[Fe(CN)_6]^{4-}$ per unit cell [12,13]. These two properties, besides its first-rate electrochemical behavior, good reversibility, natural abundant, and low cost, encouraged its evaluation as a new type of pseudocapacitive material [14–19].

The principal opposition to using PB as an electrode material is the instability in the alkali solution and insignificant cycling properties, which limits its use in supercapacitors. In contrast, conducting materials such as conducting polymer and carbon materials have good stability and high capacitance. Thus, the conducting polymer and carbon

* Corresponding author.
E-mail address: asmaa.ali@fsc.bu.edu.eg (A.A.I. Ali).

https://doi.org/10.1016/j.est.2023.108056
Received 4 April 2023; Received in revised form 25 May 2023; Accepted 11 June 2023
Available online 23 June 2023

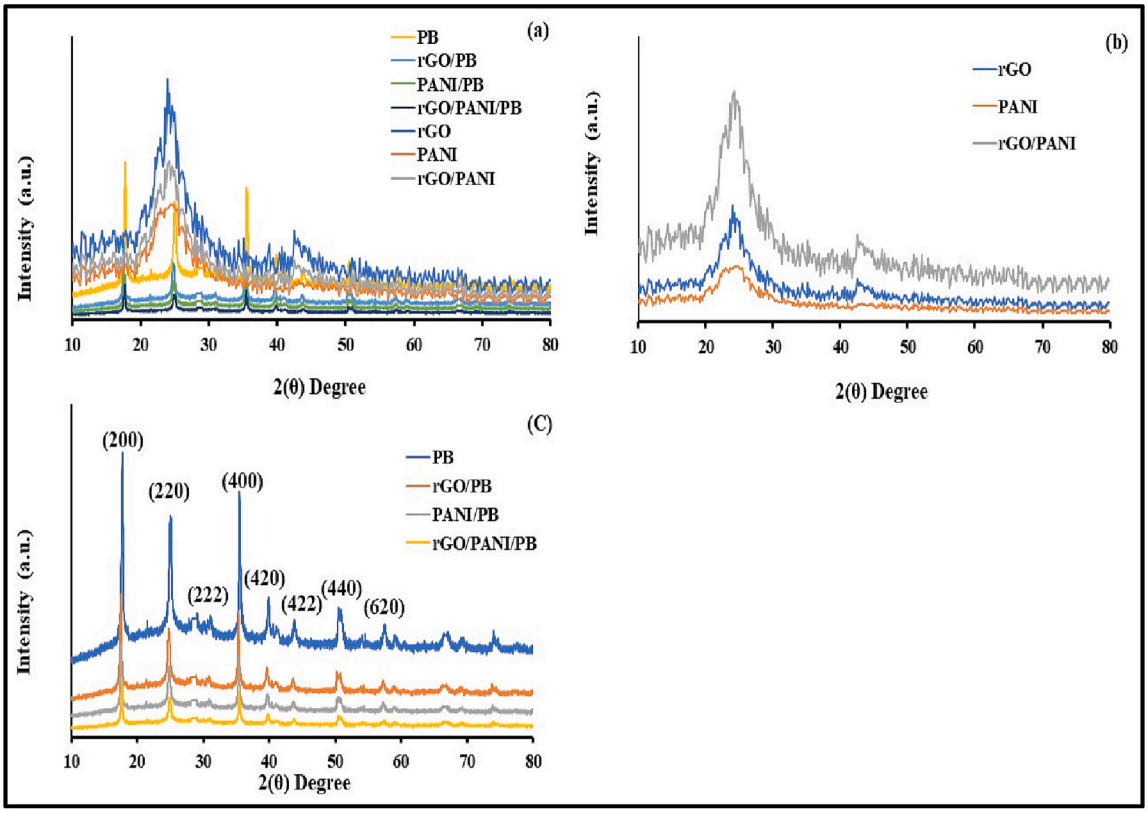

Fig. 1. XRD of investigated samples.

materials protected PB composite may increase the stability of PB. Reduced graphene oxide (rGO) is one of the most interesting carbonaceous materials for EDLC electrodes because of its porous structure and specific surface area, outstanding electronic conductivity, and substantial theoretical specific capacitance [20]. Polyaniline (PANI), as one of conducting materials, has drawn wide interest due to its respectable electrochemical, thermal, and environmental stabilities, low cost, distinguished conductivity, and high theoretical specific capacitance [21,22]. The pseudo-capacitance of PANI makes it an encouraging applicant for electrochemical capacitor applications [23]. Thus, supercapacitors with prominent capacitance and good cycling stability can be constructed using the advantages of the rGO, PANI, and PB with various valence states.

In the present work, we have prepared individual and different PB, rGO, and PANI film hybrids by employing electrodeposition, electropolymerization, and simple chemical methods. Various characterization methods have successfully investigated the interactions between the individual components of the prepared composites. The energy storage of the prepared materials was studied. The triple composite film of rGO/PANI/PB showed significantly improved energy storage capabilities compared to the pristine PANI, PB, and rGO, as well as their binary composites revealing the synergetic effects of the individual components. The highest capacitance rGO/PANI/PB electrode was used as a positive electrode in an asymmetric supercapacitor (ASC) with activated carbon (AC) as a negative electrode. A two-electrode arrangement was used to assess electrochemical performance.

2. Materials and methods

2.1. Chemicals and synthesis

Exception for aniline, all the chemicals were of analytical quality and employed without additional purification. Prior to usage, the aniline was distilled at reduced pressure. Activated carbon (AC) with a surface area of 1100 m^2/g was provided from Jiangsu Zhuxi Activated Carbon Co., Ltd. All samples, except reduced graphene oxide, were electrically synthesized. The electrochemical capacitors' working electrodes were made using the following methods:

(1) A modified Hummers' approach was used to create a reduced graphene oxide (rGO) [24].
(2) Polyaniline thin film was deposited using the electrochemical polymerization method on FTO Glass. This was accomplished by doing five cycles of back-and-forth scanning from 0 to +1.2 V vs. SCE at a scan rate of 50 mV/s in an aqueous solution containing 0.5 M H_2SO_4 and 0.5 M aniline [25].
(3) Prussian Blue Film was deposited on FTO glass substrate by Chronoamperometry at potential −0.5 V for 10 min from deposition solution composed of 100 mL distilled water, 0.7455 g KCl (1 M), 3.29 g of $K_3[Fe(CN)_6]$ (1 M), 2.70 g $FeCl_3.6H_2O$ (1 M).
(4) PANI/PB composite electrode was synthesized by deposition of PB on the surface of PANI film by chronoamperometry at potential −0.5 V for 10 min from a deposition solution composed of 100 mL distilled water, 0.7455 g KCl (1 M), 3.29 g $K_3[Fe(CN)_6]$ (1 M), 2.70 g $FeCl_3.6H_2O$(1 M).
(5) rGO/PANI composite electrode was prepared by deposition of rGO on FTO glass using the spin coating method. Then PANI was deposited on rGO by polymerization of aniline by chronoamperometry at potential +0.8 V for 5 min from a deposition solution containing 50 mL of 0.5 M H_2SO_4 aqueous solution comprising 0.5 M aniline.
(6) rGO/PB composite electrode was prepared by depositing PB on rGO/FTO surface by chronoamperometry at potential −0.5 V for 10 min from deposition solution composed of 100 mL distilled water, 0.7455 g KCl (1 M), 3.29 g of $K_3[Fe(CN)_6]$ (1 M), 2.70 g $FeCl_3.6H_2O$ (1 M).
(7) rGO/PANI/PB composite electrode has been prepared by electropolymerization of aniline on the rGO/PB/FTO surface by

chronoamperometry at potential +0.8 V for 5 min from deposition solution containing 50 mL of 0.5 M H_2SO_4 aqueous solution enclosing 0.5 M aniline.

All the prepared samples were left to dry in the air naturally overnight before making the electrochemical measurements.

2.2. Characterization tools

The crystal structure of as-synthesized materials was investigated by using an X-ray diffractometer (XRD, D8 Discover SSS, Bruker, the Netherlands, CuKα radiation with wavelength $\lambda = 0.154$ nm) in the 2θ range from 5° to 80°. The attenuated total reflectance Fourier-transform infrared spectroscopy (Vector 22, Bruker Inc., Billerica, MA, USA) was employed to identify functional groups of the thin films in the 4000–400 cm^{-1} range. The examined materials' Brunauer-Emmett-Teller (BET)-specific surface area and pore properties were determined using a Micrometrics ASAP 2020 analyzer and nitrogen adsorption-desorption isotherms at 77 K. The morphologies of the materials were examined using SEM (JEOL JSM-6460, Tokyo, Japan).

2.3. Electrochemical measurements

Electrochemical measurements were carried out in a three-electrode cell employing a working electrode, a platinum wire with a high area dimension electrode, and saturated calomel reference electrode. To make the working electrodes, a homogenous slurry of the studied materials, acetylene black, and polyvinylidene binder, with a weight ratio of 80: 10: 10, respectively, was formed. With a blade, the slurries were coated onto nickel foam current collectors. To avoid material degradation in the electrolyte solution, the thin layer of tested materials was coated by a Nafion membrane (prepared from Nafion solution 9/1 *v*/v in ethanol). The electrode was then dried at room temperature for three hours. All the electrochemical measurements were conducted on a potentiostat/galvanostat (Autolab 101) electrochemical workstation equipped with NOVA software. The EIS data was collected at an open-circuit potential within the frequency range of 10 mHz to 100 kHz. All measurements were done at room temperature.

Using a two-electrode pneumatic coin cell, the electrochemical properties of an asymmetric device (rGO/PANI/PB//AC). Electrolyte membrane made of LiTFSi-soaked PTFE was used as separator.

3. Results and discussion

3.1. Characterization

XRD investigated the phase purity and crystal structure of the studied materials, Fig. 1. As the XRD patterns of rGO, Fig. 1. a, b, illustrate broad reflections at 2θ ~ 24° matching to an interplanar space of 0.37 nm and which is greater than the graphite interlayer distance (0.34 nm), demonstrates the intercalation of numerous distinct oxygen-containing groups inside the interlayer gap [24]. The XRD spectrum of the PANI (Fig. 1.a, b) displays a wide peak in the range of 15-25°, indicating that the PANI exhibit amorphous nature. The XRD patterns of PB, Fig. 1.a, c, show diffraction peaks at 17.71°, 24.9°, 31.33°, 35.5°, 39.75°, 43.58°, 51.27°, and 57.64° which are assigned to the (200), (220), (222), (400), (420), (422), (440) and (620) crystal planes of the Prussian Blue, respectively. These peaks can be related to the face-centered cubic structure of PB (JCPDS 73–0687, space group Fm3m, a = b = c = 10.13 Å, α = β = γ = 90°). The binary and ternary systems' XRDs show peaks corresponding to all component materials' standard diffraction data. The peak intensities of (200) and (400) of PB in the composite samples have been reduced and shifted to a lower degree due to the introduction of rGO and/or PANI into the PB.

The average crystallite size of the examined materials was determined through Scherrer's relation [26]:

Table 1
Particle size, surface area and pore size of the studied materials.

Sample	Particle Size, nm	Surface area, m^2/g	Pore Size, nm
PB	35	50	4.3
rGO	–	171	6.5
PANI	–	42	4.9
rGO/PANI	–	192	6.1
rGO/PB	25	182	7.0
PANI/PB	28	190	7.9
rGO/PANI/ PB	20	208	10.9

$$D^{/} = \frac{0.9\lambda}{\beta\, cos\, \theta} \quad (1)$$

where λ denotes the X-ray wavelength employed, θ signifies the angle of incidence of X-rays, and β denotes the diffraction peak's half-peak width. The acquired outcomes are listed in Table 1, demonstrating that the particles of all the materials fall within the nanometer scale range.

Fig. 2 illustrates the SEM images of the prepared samples. The micrograph of the rGO Fig. 2.a showed transparent and ultrathin paper-like morphology. The SEM image of PANI Fig. 2.b shows a morphological structure composed of deformed nanospheres. The SEM image of PB Fig. 2.c demonstrates a mixed morphological structure with the popularity of deformed spheres.The micrographs of the binary and ternary composites, Fig. 2.d-g, show mixed morphological structures of the basic materials. It could be seen that the PB particles were covered by each of the PINI and rGO nanofiber sheets in each binary and ternary system.

Fig. 3 show the FTIR spectra of the studied materials. The FTIR spectrum of rGO demonstrates a peak at 3450 cm^{-1} apportioned to the hydroxyl compound functional group (–OH) besides peaks at 1628 and 1239 cm^{-1} assigned to the aromatic carbon functional group (C=C) and epoxy functional group (–CO), respectively [27]. All the samples containing rGO also showed absorption bands at ~3390 and 1590 cm^{-1} assigned to the O—H stretching and H-O-H bending modes [28], respectively, revealing the existence of adsorbed and interstitial water in the samples. The pure Prussian blue demonstrates an intense peak at ~2070 cm^{-1}, credited to the stretching absorption band of the CN group in the Fe^{2+}-CN-Fe^{3+} [29]. This band is also detected in the spectra of the binary and ternary composites containing PB. The FT-IR spectra of the samples containing PANI demonstrate peaks at ~1479 cm^{-1} credited to the quinoid ring's C = C stretching vibration [30].

The surface area analysis using N_2 adsorption and desorption measurements of the investigated samples at 77 K, Fig. 4, provides essential information about the surface and pore-size distribution, which are the main important factors for electroactive materials in energy conversion/storage appliances [31]. According to the findings, all samples, except PANI, contain hysteresis loops, including capillary condensation ($P/P^{\circ} > 0.43$). According to the IUPAC classification, the hysteresis loop of PANI begins at $P/P^{\circ} > 0.90$ and may be classified by the type V with H1 referring to a prominent organization of pore size regularity and disclosing to the mesoporous structures. BET surface areas and mean pore diameters were calculated using desorption data [32] and are presented in Table 1, which demonstrates that the specific surface rises in the following order:

rGO/PANI/ PB > rGO/PB > rGO > PANI/PB > rGO/PANI > PB > PANI. Whereas the pore size diameter follows the order: rGO/PANI/ PB > rGO/PB > PANI/PB > rGO/PANI > rGO > PANI > PB.

3.2. Electrochemical properties of the synthesized electrodes

The CV plots of the as-synthesized electrodes recorded in 2 M Na_2SO_4 electrolyte solution at a sweep rate of 10 mV/s are shown in Fig. 5. The CV plot of rGO demonstrates an almost rectangular form denoting a dielectric behavior. The CV voltammogram of PANI displays two pairs of redox peaks as a result of leucoemeraldine ↔ emeraldine and

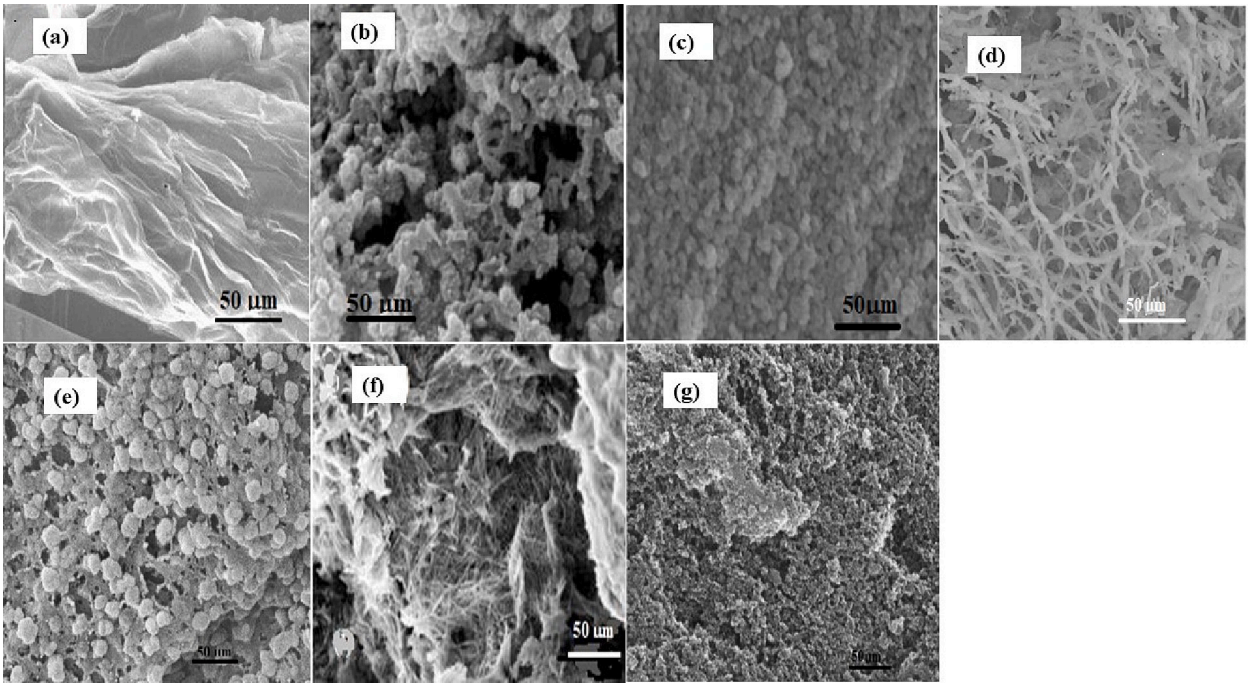

Fig. 2. SEM of (a) rGO, (b) PANI, (c) PB, (d) rGO/PANI, (e) PANI/PB, (f) rGO/PB and (g) rGO/PANI/PB.

emeraldine ↔ pernigraniline redox conversions. The acid-doped version, i.e., the emeraldine structure, is the most conducting of these structures. The observed reversible redox pairs refer to the pseudocapacitance behavior of PANI [33]. The CV voltammogram of the electrodes containing PB demonstrated clear symmetric redox peaks, indicating that the electrochemical process was reversible. The redox course of the Fe (II/III) couple coordinated through nitrogen atoms from the C—N group (Eq. (2)) may be the cause of a pair of redox peaks that appeared at about 0.2 V [34].

$$Fe^{3+}\left[Fe^{3+}(CN)_6\right] + Na^{+} + e - \rightarrow Na\,Fe^{2+}\left[Fe^{3+}(CN)_6\right] \quad (2)$$

Fig. 5 also shows that the redox peaks obtained from the CV rGO/PB, PANI/PB, and rGO/PANI/PB electrodes are higher than that obtained from PB, referring to a synergistic effect between the PB and each of rGO and PANI. The large CV current obtained for the composite electrode materials indicate that they have high conductivity and low internal resistance. The anodic and cathodic PB peaks are found in the CV curves of the PB electrode at 340 and 120 mV, respectively. About 220 mV is the potential peak separation (ΔE_P). At the same time, the CV plots of the binary and ternary electrodes have similar redox peaks with smaller ΔE_P values of 180, 190, and 180 and 175 mV for rGO/PB, PANI/PB, and rGO/PANI and rGO/PANI/PB, respectively. These outcomes illustrate that the electron transfer rate is significantly increased while the overpotential of the Fe(II/III) redox course at the binary and ternary electrodes is noticeably reduced.

The specific capacitances (C_{sp}) were estimated from the CV plots according to the following equation [35].

$$C_{sp} = \frac{\int i\,dV}{2m\nu\Delta V} \quad (3)$$

where $\int i\,dV$ is the integral region of the CV peak, ΔV is the potential window, m is the active material's loading mass, and ν is the sweeping rate. The acquired results are recorded in Table 2, which shows that the specific capacitance of ternary composite is greater than that of binary and single materials.

The performance in capacitance of binary and ternary composites Table 2 can be explained based on the existence of a detectible amount of the rGO, which causes an enhancement in the number of mesopores that the electrolyte's Na^{+} can enter. Besides, the great conducting network arranged by rGO and PANI causes development in the electron transport for the time of the charge and discharge processes, accordingly intensifying the electrical conductivity and charge transport tracks produced in PB. The non-rectangular style of the CV plots of all samples containing PB and/or PANI indicates that pseudocapacitance contributes significantly to the overall specific capacitance.

Generally, besides the manifestation of carbon in rGO, the PANI molecules allowed better conductivity from π-electron bonds. Moreover, the great quantity of oxygen, a greatly electronegative element, leads us to be sure that the composites are highly conducting materials. Also, the existence of oxygen and nitrogen groups in rGO and polyaniline increases the surface hydrophilicity in an aqueous electrolyte and enhances the double-layer capacitance qualities of the composites. In conclusion, the interaction between the Fe ions in PB and the polar molecules in rGO and PANI results in a pseudocapacitor's charge transfer properties, which enhance overall storage [36]. Because of all these characteristics, upgraded specific capacitance was achieved by rGO/PANI/PB nanocomposite.

More reasons for the synergetic impact of rGO, PANI, and PB may be found in the following. For example, rGO nanosheets are uniformly distributed on PB and PANI, allowing the electrolyte to penetrate. Furthermore, the use of rGO lowers PB particle agglomeration, improving their electrochemical utilization. This finding further implies that the rGO nanosheets served as a mechanical and electrical bridge between the PB nanoparticles in the composite structure during the charging/discharging operations. Furthermore, the polymerization of PANI forms well-arranged and uniformly distributed nanoparticles on the rGO/PB via hydrogen bonding and electrostatic interactions (confirmed by FT-IR data), reducing electrically isolated parts that cannot be used and providing a significant electrochemically high active surface area for charge transfer. Based on BET data, this highly porous shape can suggest a short diffusion channel length and extra active sites for electrolyte ions/electrons, maximizing electrode material utilization and leading in fast charging/discharging rates.

The GCD analysis is the more practical method for understanding the super capacitive characteristics of a material. The GCD plots of the as-prepared electrodes in 2 M Na_2SO_4 electrolyte were recorded in the

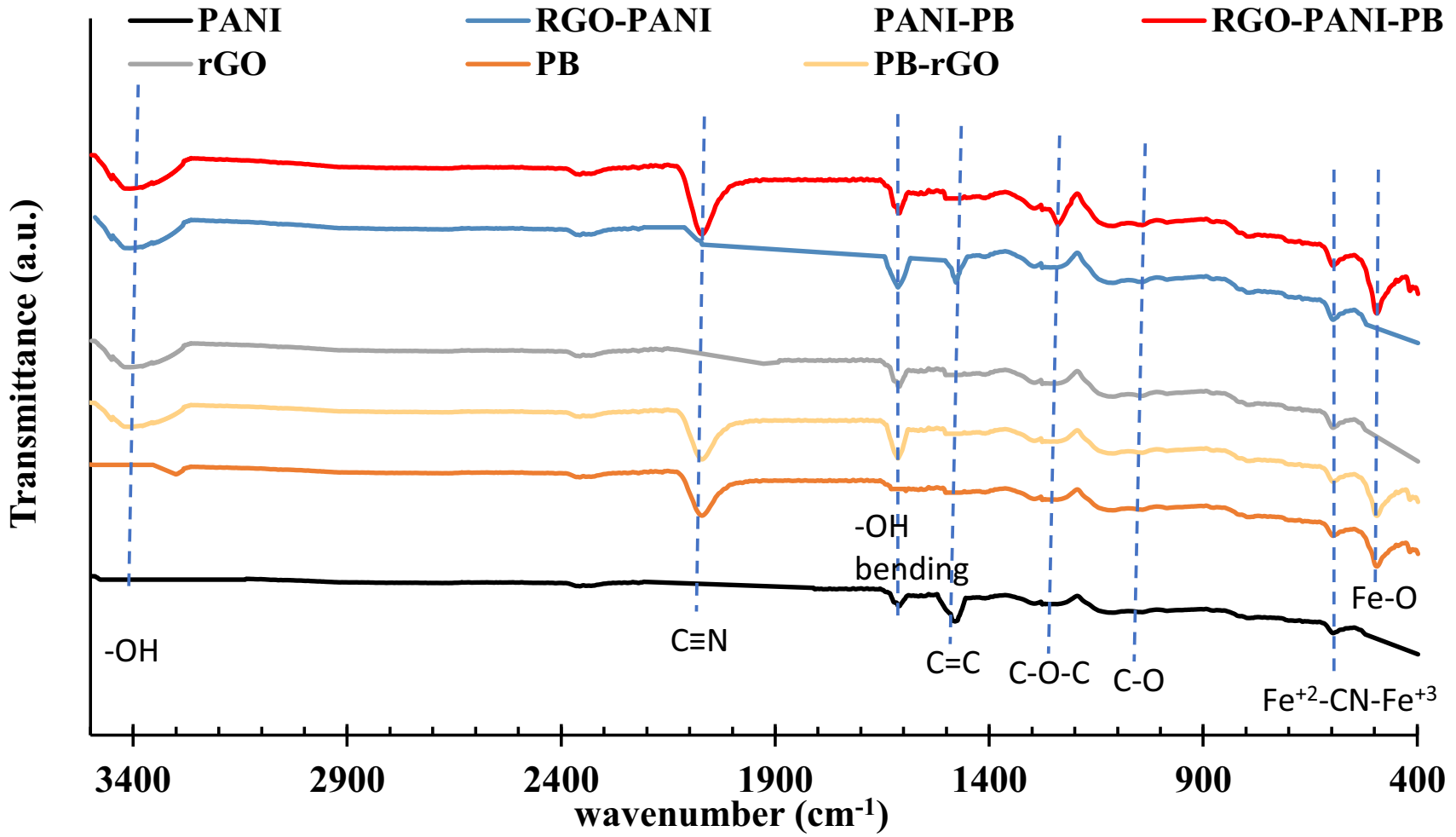

Fig. 3. FT-IR of the investigated samples.

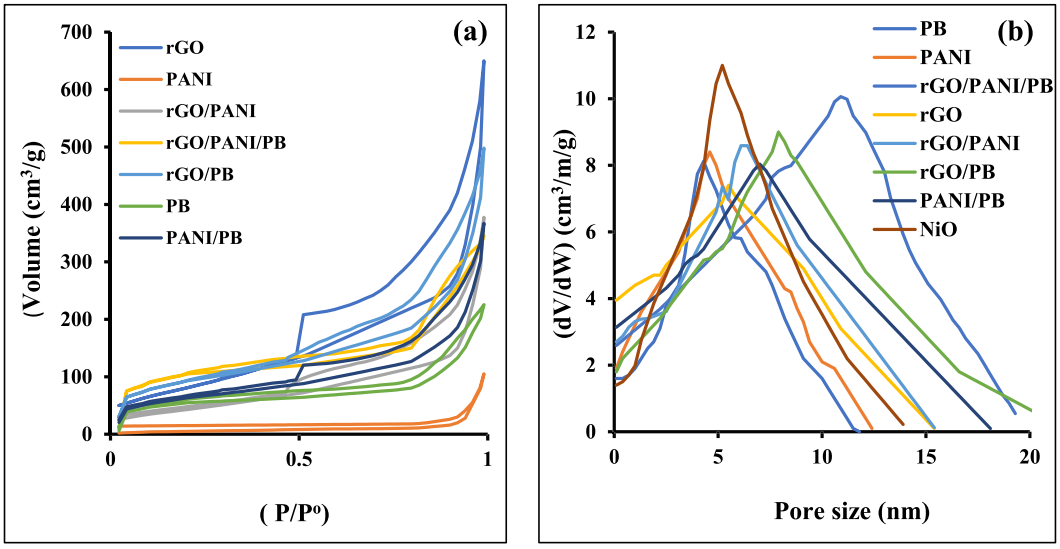

Fig. 4. (a) N_2 adsorption/desorption isotherm (b) and pore size distribution of the investigated samples.

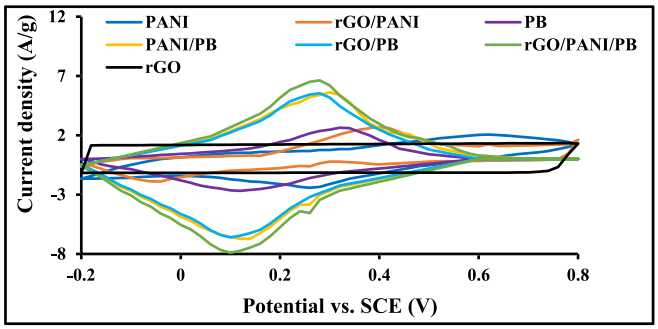

Fig. 5. CV of all investigated electrodes in 2 M Na_2SO_4 electrolyte at a scan rate 10 mV/s.

Table 2
Specific capacitance of the studied samples using CV and GCD.

Sample	Specific capacitance C_{sp}, F/g				
	From CV at 10 mV/s	From GCD at			
		1A/g	2A/g	5A/g	10A/g
PB	87	85	82	81	80
rGO	125	120	115	112	111
PANI	77	75	74	72	69
rGO/PANI	150	145	143	140	138
PANI/PB	212	207	205	201	195
rGO/PB	203	199	195	191	187
rGO/PANI/PB	340	336	330	325	321

voltage range − 0.2 - 0.8 V at a current density of 1 A/g as presented in Fig. 6. It is noted that the discharging curve of rGO electrode exhibits an ideal linear curve, which points out to the double layer capacitance behavior. However, in all the other electrodes, the charging/discharging curves are not symmetrical, demonstrating the pseudo-capacitive behavior of electrode material. rGO/PANI/PB electrode has a significantly longer discharge time and smallest potential drop (IR) than the other materials electrode; consequently, it has the most excellent specific capacitance in all tested electrodes. The C_{sp} values were determined from the discharge curves using the formula [37].

$$C_{sp} = \frac{I\,\Delta t}{m\Delta V} \quad (4)$$

where I denotes the discharge current, Δt denotes the discharge duration, m is the loading mass and ΔV is the voltage change of the electrode materials in the course of the discharge process. The acquired outcomes are listed in Table 2, which confirms our prediction that the rGO@PANI@PB electrode has an elevated capacity value due to the synergistic effect of its constituents, as mentioned above. These results also provide credence to the earlier computed specific capacitances based on CV curves.

Galvanostatic charge-discharge analyses were also carried out by employing a series of charging and discharging currents (1–10 A/g) to the supercapacitors. Table 2 shows the results showing that the electrode capacitance falls as the current density raises. The presence of active interior sites cannot entirely strengthen the redox transition at high current density owing to the diffusion influence of the Na^+ inside the electrode [38,39].

Cycling stability, which can be communicated in the relationship of capacitance retention (%), is an important feature that defines the efficiency and durability of supercapacitors. Thus, the tested electrodes' capacitance retention (%) was evaluated through 3000 GCD cycles at 1 A/g current density, as illustrated in Fig. 6. b. The capacitive retentions are found to be: 92 %, 89.7 %, 88.9 %, 86.6 %, 77.5 %, 75.3 %, and 75 % for rGO/PANI/PB, PANI/PB, rGO, rGO/PB, rGO/PANI, PANI, and PB, respectively. The synergistic interactions between its components may be responsible for the high stability of rGO/PANI/PB, where the rGO, which acts as a protective layer, induces some mechanical deformation during the redox process of the PB particles [40].

The EIS analysis is an effective and helpful method for assessing the conductivity and charge transport characteristics at the film/electrolyte interface [41]. Fig. 6. c demonstrates the Nyquist plot (imaginary impedance, Z/ vs. real impedance, Z/) of the impedance response of the tested electrodes in the frequency range of 10 kHz to 0.01 Hz. For each plot, a depressed semicircle in the figure's high-frequency section is connected to a sloped line in the low-frequency area. The inset of Fig. 6. c. shows the EIS at higher frequencies. The intercepts on the Z'−axis are labelled as solution resistance (R_s), and the diameters of semicircles specify electrode resistance (R_{ct}) in the high-frequency region due to charge transfer resistance in the active materials [42]. For the investigated electrodes, R_{ct} was found to follow the order:

Ternary electrode < PANI/PB < rGO/PB < rGO/PANI < rGO < PANI <PB.

A curvature line close to 45° is detected in the low-frequency section of the Nyquist plot. This is ascribed to the Warburg impedance linked to the diffusion/ transport of Na^+ ions and the pores of the electroactive

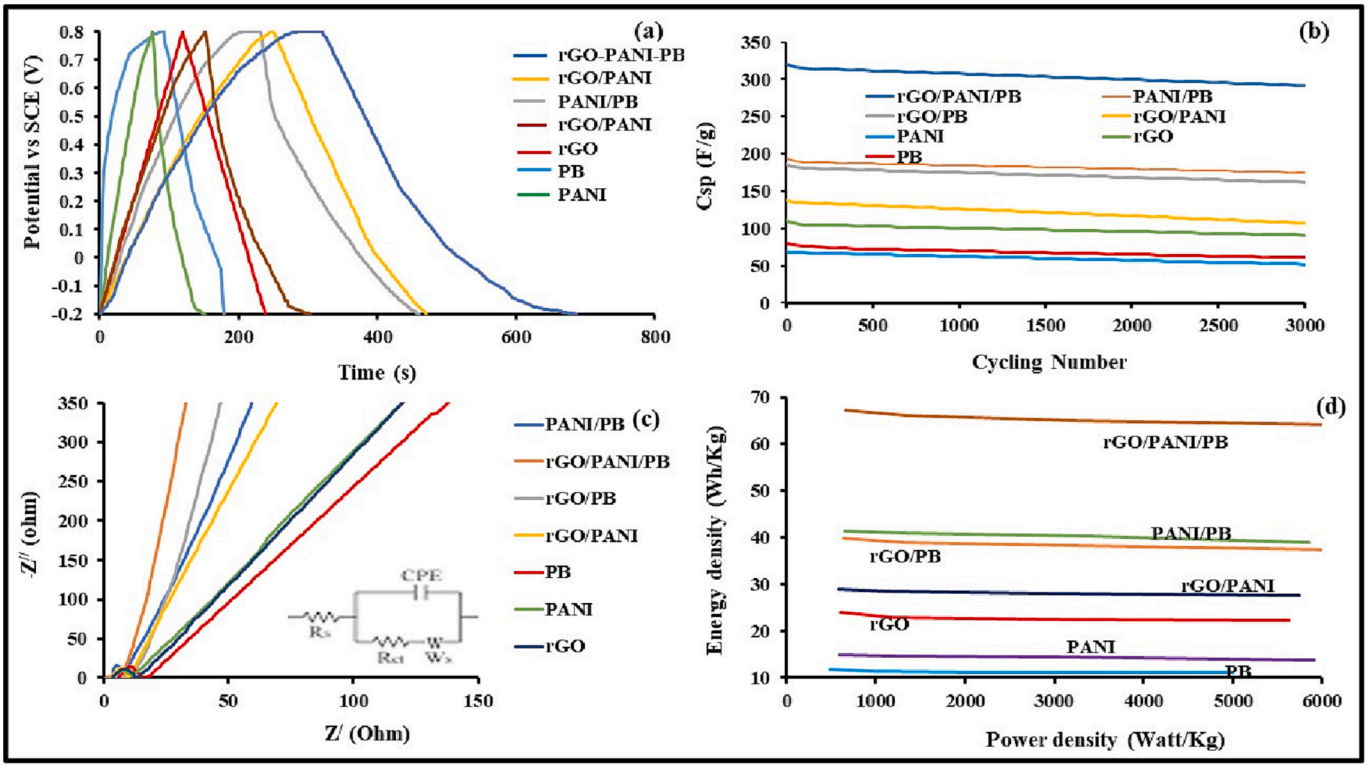

Fig. 6. (a) The GCD curves of all the investigated electrodes in 2 M Na_2SO_4 electrolyte at discharging current density of 1A/g. (b) The cycling stability of the investigated electrodes at 1 A g^{-1}. (c) The Nyquist impedance plots of the investigated electrodes and their equivalent electric circuit, (d) Ragone plots of the investigated electrodes.

Table 3
Parameters values from the fitted impedance equivalent circuit of the investigated electrodes.

Sample	rGO	PANI	PB	rGO/PB	PANI/PB	rGO/PANI	rGO/PANI/PB
R_s (Ω)	3.13	5.49	5.52	3.11	3.31	2.62	0.91
R_{ct} (Ω)	9.91	10.78	11.11	5.62	4.52	7.11	4.51
W (Ω)	14.21	17.32	18.35	9.37	7.91	10.73	5.82
C_{sp} (mF)	120.0	175.0	85.0	199	207	145	336

material throughout the redox reactions and implies that the electrolyte/electrode redox reactions were controlled by the mass transfer process, i.e., diffusion-controlled reactions. In the low-frequency area, the rGO/PANI/PB electrode displays the most significant slope of the other electrodes. This is due to the rGO/PANI/PB electrode's microporous shape, which has a large surface area to enable quick ions diffusion and electrolyte penetration in these pores, improving the specific capacitance. Based on the acquired results, the EIS data are fitted with the equivalent circuit presented in Fig. 6. c, and the simulated outcomes are recorded in Table 3.

The synergistic impact exhibited in the ternary rGO/ PANI/ PB composite electrode can also be observed from the EIS data. The ternary electrode displayed a lower equivalent series resistance R_s and charge-transfer resistance R_{ct}. This indicated that the rGO/ PANI/ PB had a substantial synergistic impact when compared to the binary composite and purity components. The decreased resistance of the rGO/ PANI/ PB electrode allows for a faster Faraday reaction, resulting in higher rate capability. Furthermore, the limited slope of the straight line demonstrated the electrolyte's diffusive resistance in the electrode pores and cation diffusion in the host materials.

To provide further information on the electrochemical performance of the studied electrodes, the Na^+ ion diffusion coefficients ($D^{/}$) in the analyzed electrodes are also computed using Eq. (5) [43].

$$D^{//} = \frac{R^2T^2}{2\,A^2n^4F^2C^2\sigma^2} \tag{5}$$

where F, R, T, represent the Faraday number, the universal gas constant, the temperature of the system, respectively. A, n and C denote the electrode surface area and the charge-transfer number and the electrolyte ion concentration, respectively. σ is the Warburg factor, which is obtained by the following equation:

$$Z^{/} = R_S + R_{CT} + \sigma\,\omega^{0.5} \tag{6}$$

where ω is the angular frequency, the evaluated Na^+- diffusion coefficients are 2×10^{-13}, 2.4×10^{-13}, 1.1×10^{-13}, 8.2×10^{-14}, 7.5×10^{-14}, 5.8×10^{-14} and 3.9×10^{-14} $cm^2\,s^{-1}$ for rGO/PANI/PB, rGO/PB, PANI/PB, rGO/PANI, rGO, PANI, and PB, respectively. Due to its substantially larger pore size and synergetic effect, which makes it easier for the electrolyte to diffuse through the composite electrode, ternary and binary composites have more significant diffusion coefficients than their constituent materials.

Power density (P_d) and energy density (E_d) are critical criteria for evaluating supercapacitor and electrode material electrochemical performance. They are computed using Eqs. (7) and (8) [40].

$$E_d = \frac{C_{sp}\,\Delta V^2}{7.2} \tag{7}$$

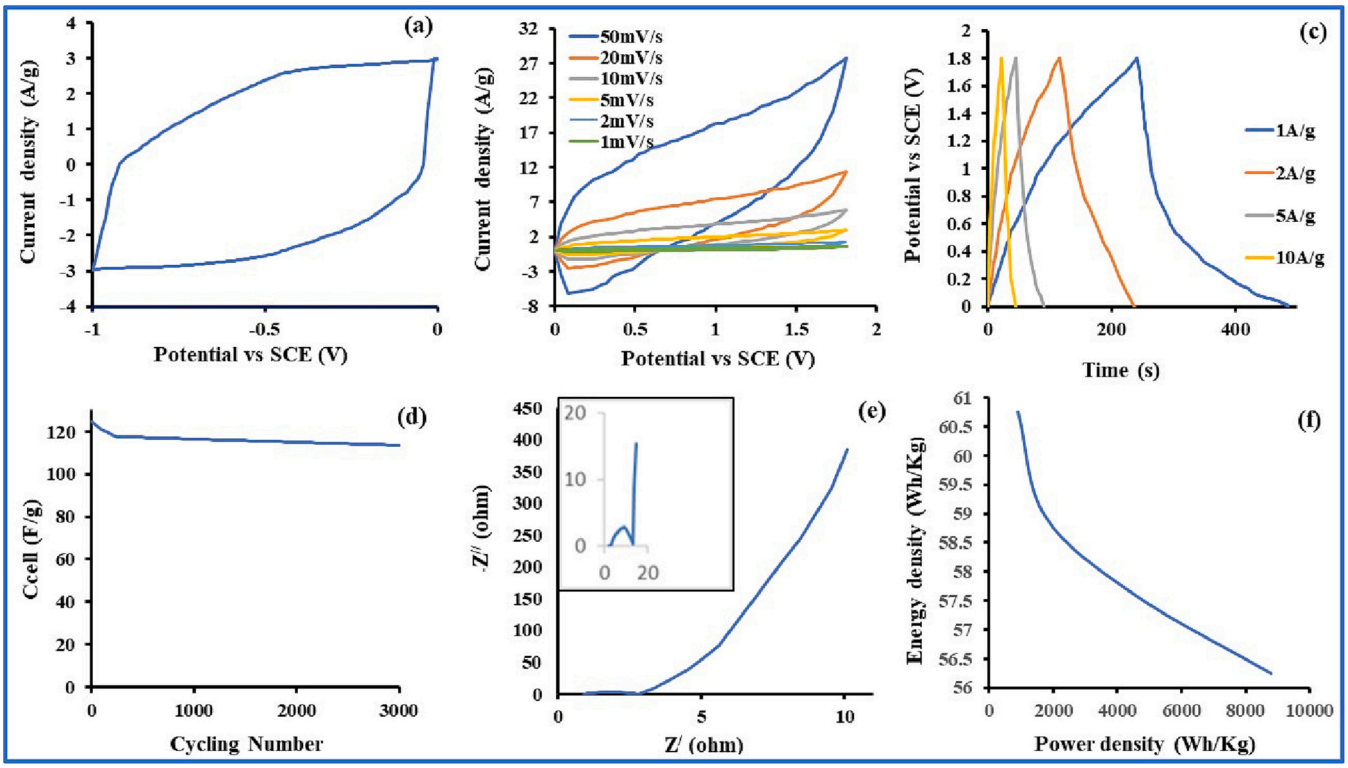

Fig. 7. (a) CV of AC at 10 mV/s (b) CV of rGO/PANI/PB //AC asymmetric cell at several scan rates, (c) the GCD plots of rGO/PANI/PB //AC asymmetric cell at different current densities, (d) stability of rGO/PANI/PB //AC asymmetric cell, (e) Nyquist plot of rGO/PANI/PB //AC asymmetric cell, and (f) Ragone plot of the asymmetric cell.

$$P_d = \frac{3600\, E_d}{\Delta t} \tag{8}$$

where ΔV and Δt are the potential windows and the discharge time, respectivel. The E_d-values of the tested electrodes at several P_d-values (Ragon plots) are demonstrated in Fig. 6.d. With a power density of 6.25 kW kg^{-1}, the rGO/PANI/PB electrode has an energy density of 64.2 Wh kg^{-1}. This demonstrates that the rGO/PANI/PB material is a promising electrode for electrochemical capacitors.

3.3. Asymmetric supercapacitor (rGO/PANI/PB//AC)

Next, we assembled the rGO/PANI/PB //AC asymmetric supercapacitor in a two-electrode setup, as discussed in the "Experimental" section. The capacitance of the AC-negative electrode was measured in a three-electrode system at a scan rate of 10 mV/s within a potential window of 1 to 0 V (versus SCE), and the outcomes are shown in Fig. 7. a. The figure depicts the electric double-layer capacitance as a rectangular form. The specific capacitance of the activated carbon electrode calculated based on Eq. (3) is 190 F/g, which is consistent with that reported in the literature [44].

Usually, asymmetric supercapacitors require to be charge-balanced (q^{+}=q^{-}) such that the applied voltage is evenly divided between the electrodes for ideal performance [45]. As a consequence, the mass balance formula (9) follows:

$$\frac{m^-}{m^+} = \frac{C_m^+}{C_m^-} x\, \frac{\Delta V^+}{\Delta V^-} \tag{9}$$

where m is the electrode's mass, C is the specific capacity, and ΔV is the potential working window of the positive/negative electrode. Consequently, the $m^-/m^+ = 1.26$ for the examined ASC, and the ASD device's best functioning window was assessed to be 0 to 1.8 V.

Fig. 7. b depicts the ASC device's CV curves at scan rates ranged from 1 to 50 mV/s. The assembled ASC exhibited stable capacitive behavior, as shown in the figure. The CV curves do not change with changing the sweep rate, demonstrating the remarkbly-electrochemical reversibility and quick charge-discharge manner. The specific capacitance (C_{cell}) of the asymmetric cell is calculated from a CV curve using Eq. (10) [46].

$$C_{cell} = \frac{\int_{-V}^{+V} I(V)dV}{2Mv\Delta V} \tag{10}$$

where M represents the mass of the active materials in the two electrodes and all other symbols are as specified above. The evaluated specific capacity of the device from the GCD measurements is found to decrease gradually with increasing the scan rate, i.e., 144, 142, 139, 136,132, and 129 F/g, at scan rates of 1, 2, 5, 10, 20, and 50 mVs^{-1}, respectively.

The GCD of the ASC was further investigated at several current densities ranging from 1 to 10 A g-1, with the findings shown in Fig. 7. c. The charge and discharge parts of the GCD plots are almost symmetric and display a small internal resistance drop, as shown in the figure. Using Eq. (11), the discharge parts of the GCD draws were used to compute the associated specific capacity (C_{cell}) of the device at various particular currents (I) [47,48].

$$C_{cell} = \frac{Idt}{MdV} \tag{11}$$

At 1, 2, 5, and 10 Ag^{-1}, the C_{cell} calculated is 135, 131, 128, and 125 Fg^{-1}, respectively. With a 10-fold increase in current density, the ASC's capacitance remains at 92.5 %, indicating a reasonable ability rate. This may be due to the extraordinary nanostructure features with large surface area and good electrical conductivity of the activated carbon electrode, which promote excessive adsorption of electrolyte as well as an efficient ion intercalation/deintercalation.

The cyclic stability of the device is performed at a current density of

Table 4
Compares electrochemical data from different asymmetric supercapacitor configurations published in the literature with data from the current study.

Material	E_d (Wh kg^{-1})	P_d (W kg^{-1})	Ref.
$Cu(OH)_2/Cu_7S_4$//AC	48.1	429.3	[50]
$CuCoFe_2O_4$ //AC	7.9	1712	[51]
MnCoS//AC	36.9	750	[52]
Ni-Co-O@rGO-s//AC	39	7500	[53]
NiO//AC	52.4	800	[54]
$Ni_{1.64}Co_{2.40}S_4$ / rGO//AC	47.2	200	[55]
$Ni/Ni_{1.4}Co_{1.6}S_2$//AC	25	10,800	[56]
rGO/PANI/PB //AC	56.3	8804	This work

10 A g^{-1} for 3000 cycles. Fig. 7(d) demonstrates a high capacity retention of ~91 %. EIS was performed further to explore the improved capacitive performance of the asymmetric capacitor. The resulting Nyquist plots were presented in Fig. 7e. The Figure illustrates a depressed semicircle in the high frequency region, following by an essentially straight line in the low frequency section, indicating an extremely low R_s- and R_{ct}- values of 0.91and 1.76 Ω, respectively.

The E_d- and P_d –values of the ASC were assessed by Eqs. (8) and (12) [49].

$$E_d = C_{cell}\,(\Delta V)^2/7.2 \tag{12}$$

All of the symbols have already been stated. The results generated at various current densities are depicted as a Ragone plot in Fig. 6f, which shows the most significant value of E_d is 56.3Whkg^{-1} and the highest value of P_d is 8804 Wkg^{-1}. Table 4 compares Ragone values for several systems to our results.

4. Conclusions

In summary, Prussia blue, rGO, polyaniline, and a binary and ternary composite of them are synthesized and characterized via XRD, FTIR, BET, and SEM. The prepared materials were examined as potential materials for supercapacitor electrodes. Microstructural investigation confirms the formation of the examined materials in diverse morphological structures. They all showed nanosized particles with a mesoporous structure that enables the transfer of electrolyte ions. The super capacitive performance of the investigated material was studied in 2 M Na_2SO_4 employing CV, GCD, and EIS in a three-electrode cell arrangement. The CV voltammograms have illustrated that all the materials, except rGO, show a pseudocapacitive behavior with specific capacitance following the order: rGO/PANI/PB > PANI/PB > rGO/PB > rGO/PANI > rGO > PANI > PB. The rGO/PANI/PB composite electrode has a high specific capacitance of 236 F/g at the current density of 1 A g^{-1}. It also has good cycling stability, with capacitance retention of 92 % even after 3000 cycles. It showed excellent cycling stability with capacitance retention reaching ~92 % even after 3000 cycles. The ASC device, comprised of AC negative and rGO/PANI/PB positive electrodes, has a comparatively high energy density of 56.3 Wh kg^{-1} and a power density of 8.8 kW kg^{-1} while maintaining outstanding cycling permanence (keeps 92.5 % capacitance preservation after 3000 cycles). Our findings show that the porous ternary nanocomposite of rGO/PANI/PB (a low-cost material) has a prospective use in energy storage devices.

Declaration of competing interest

The authors declared no conflicts of interest.

Data availability

Data will be made available on request.

References

[1] H. Lyu, Y. Li, C.J. Jafta, C.A. Bridges, H.M. Meyer, A. Borisevich, M. P. Paranthaman, S. Dai, X.G. Sun, Bis(trimethylsilyl) 2-fluoromalonate derivatives as electrolyte additives for high voltage lithium ion batteries, J. Power Sources 412 (2019) 527.

[2] L. Zhang, Q. Zhang, H. Xie, J. Guo, H. Lyu, Y. Li, Z. Sun, H. Wang, Z. Guo, Electrospun titania nanofibers segregated by graphene oxide for improved visible light photocatalysis, Appl. Catal. B Environ. 201 (2017) 470.

[3] J. Liu, S. Guo, C. Hu, H. Lyu, X. Yan, Z. Guo, Advanced nanocomposite electrodes for lithium-ion batteries, Multifunction Nanocomposites Energy Environ. Appl. 1 (2018) 7.

[4] H. Lyu, J. Liu, S. Qiu, Y. Cao, C. Hu, S. Guo, Z. Guo, Carbon composite spun fibers with in situ formed multicomponent nanoparticles for a lithium-ion battery anode with enhanced performance, J. Mater. Chem. A 4 (2016) 9881.

[5] C. Hu, S. Qiu, G. Lu, H. Cao, H. Lv, S. Guo, J. Liu, Enhanced electrochemical performance of barium hexaferrite nanoplates by Zn^{2+} doping serving as anode materials, RSC Adv. 5 (2015) 70749.

[6] G. Wang, L. Zhang, J. Zhang, A review of electrode materials for electrochemical supercapacitors, Chem. Soc. Rev. 41 (2012) 797–828.

[7] Y. Zhang, Y. Huang, V. Srot, P.A. van Aken, J. Maier, Y. Yu, Enhanced pseudocapacitive contributions to high-performance sodium storage in TiO_2/C nanofbers via double efects of sulfur modifcation, Nano-Micro Lett. 12 (2020) 165, https://doi.org/10.1007/s40820-020-00506-1.

[8] J.H. Lee, G. Yang, C.H. Kim, R.L. Mahajan, S.Y. Lee, S.J. Park, Flexible solid-state hybrid supercapacitors for the internet of everything (IoE), Energy Environ. Sci. 15 (2022) 2233, https://doi.org/10.1039/D1EE03567C.

[9] H. Mothkuri, H. Gupta, P.K. Jain, S. Chakrabarti, Reduced graphene oxide and MnO_2 nanoflower hybrid as an efficient electrode material for supercapacitor application, J. Miner. Sci. Mater. 1 (2020) 1005.

[10] S. Rajagopal, R.P. Vallikkattil, M.M. Ibrahim, D.G. Velev, Electrode materials for supercapacitors in hybrid electric vehicles: challenges and current progress, Condens. Matter. 7 (2022) 6, https://doi.org/10.3390/condmat7010006.

[11] K.H. Park, D.Y. Choi, J.H. Park, C. Kim, T.Y. Kim, J.W. Lee, Characterization and application of electrospun Prussian blue nanofibers synthesized by electrospinning polyacrylonitrile solution, Int. J. Electrochem. Sci. 11 (2016) 1472.

[12] P. Nie, L.F. Shen, G. Pang, Y.Y. Zhu, G.Y. Xu, Y.H. Qing, H. Dou, X.G. Zhang, Flexible metal–organic frameworks as superior cathodes for rechargeable sodium-ion batteries, J. Mater. Chem. A 3 (2015) 16590.

[13] A. Mullaliu, J.A.G. Asenbauer, S. Passerini, M. Giorgetti, Highlighting the reversible manganese electroactivity in Na-rich manganese hexacyanoferrate material for Li- and Na-ion storage, Small Methods 4 (2019) 1900529.

[14] E.S. Goda, S. Lee, M. Sohail, K.R. Yoon, Prussian blue and its analogues as advanced supercapacitor electrodes, J. Energy Chem. 50 (2020) 206–229.

[15] Y. Yue, Z. Zhang, A.J. Binder, J. Chen, X. Jin, S.H. Overbury, S. Dai, Hierarchically superstructured Prussian blue analogues: spontaneous assembly synthesis and applications as pseudocapacitive materials, Chem. Sus. Chem. 8 (2015) 177.

[16] Y. Lin, L. Zhang, Y. Xiong, T. Wei, Toward the design of high-performance supercapacitors by Prussian blue, its analogues and their derivatives, Energy Environ. Mater. 3 (2020) 323–345, https://doi.org/10.1002/eem2.12096.

[17] A. Kumar, D. Das, D. Sarkar, S. Patil, A. Shukla, Supercapacitors with Prussian blue derived carbon encapsulated Fe/Fe_3C nanocomposites, J. Electrochem. Soc. 167 (2020), 060529, https://doi.org/10.1149/1945-7111/ab838f.

[18] G. Han, Y. Liu, E. Kan, J. Tang, L. Zhang, H. Wang, W. Tang, Sandwich-structured MnO_2/polypyrrole/reduced graphene oxide hybrid composites for high-performance supercapacitors, RSC Adv. 4 (2014) 9898.

[19] K. Liang, T. Gu, Z. Cao, X. Tang, W. Hu, B. Wei, In situ synthesis of SWNTs@MnO_2/polypyrrole hybrid film as binder-free supercapacitor electrode, Nano Energy 9 (2014) 245.

[20] J. Yan, Z. Fan, W. Sun, G. Ning, T. Wei, Q. Zhang, R. Zhang, L. Zhi, F. Wei, Advanced asymmetric supercapacitors based on $Ni(OH)_2$/graphene and porous graphene electrodes with high energy density, Adv. Funct. Mater. 22 (12) (2012) 2632.

[21] S. Bhadra, D. Khastgir, N.K. Singha, J.H. Lee, Progress in preparation, processing and applications of polyaniline, Prog. Polym. Sci. 34 (2009) 783.

[22] S. Bhadra, N.K. Singha, D. Khastgir, Electrochemical synthesis ofpolyaniline and its comparison with chemically synthesized polyaniline, J. Appl. Polym. Sci. 104 (2007) 1900.

[23] J. Jang, J.H. Oh, Abrication of a highly transparent conductive thin film from polypyrrole/poly(methyl methacrylate) core/shell nanospheres, Adv. Funct. Mater. 15 (2005) 494.

[24] S.N. Alam, N. Sharma, L. Kumar, Synthesis of graphene oxide (GO) by modified hummers method and its thermal reduction to obtain reduced graphene oxide (rGO), Graphene 6 (2017) 1.

[25] A. Kumar, A. Kumar, H. Mudila, K. Awasthi, V. Kuma, Synthesis and thermal analysis of polyaniline (PANI), J. Phys. Conf. Ser. 1531 (2020), 012108.

[26] S. Qiu, S. Kalita, Synthesis, processing and characterization of nanocrystalline titanium dioxide, Mater. Sci Eng. A. 435–436 (2006) 327.

[27] H.I. Fathoni, K.R. Kawuni, Q.A. Hanif, S. Wahyuningsi, A. Supriyanto, Harjana, A. H. Ramelan, Effect of reaction time on the rGO-CoS composite structural properties, J. Phys. Conf. Ser. 1912 (2021), 012014.

[28] M. Acik, G. Lee, C. Mattevi, M. Chhowalla, K. Cho, Y.J. Chabal, Unusual infrared-absorption mechanism in thermally reduced graphene oxide, Nat. Mater. 9 (10) (2010) 840.

[29] S. Rajendran, R.J. Rathish, S.S. Prabha, A. Anandan, Green electrochemistry – a versatile tool in green synthesis: an overview, Electrochim. Acta 34 (2016) 321.

[30] B.S. Singu, P. Srinivasan, S. Pabba, Benzoyl peroxide oxidation route to nano form polyaniline salt containing dual dopants for pseudocapacitor, J. Electrochem. Soc. 159 (2012) A6.
[31] W. Li, L. Lei, D. Zhao, Mesoporous materials for energy conversion and storage devices, Nat. Rev. Mater. 1 (2016) 16023.
[32] Y.H. Tan, Urface area and pore size characteristics of nanoporous gold subjected to thermal, mechanical, or surface modification studied using gas adsorption isotherms, cyclic voltammetry, thermogravimetric analysis, and scanning electron microscopy, J. Mater. Chem. 22 (2012) 6733.
[33] H. Wang, Q. Hao, X. Yang, L. Lu, X. Wang, Effect of graphene oxide on the properties of its composite with polyaniline, ACS Appl. Mater. Interfaces 2 (2010) 821.
[34] Y. Zou, Q. Wang, C. Xiang, Z. She, H. Chu, S. Qui, F. Xu, S. Lui, C. Tang, L. Sun, One-pot synthesis of ternary polypyrrole Prussian-blue graphene-oxide hybrid composite as electrode material for high-performance supercapacitors, Electrochem. Acta. 188 (2016) 126.
[35] H. Li, J. Wang, Q. Chu, Z. Wang, F. Zhang, S. Wang, Theoretical and experimental specific capacitance of polyaniline in sulfuric acid, J. Power Sources 190 (2009) 578.
[36] A.N. Grace, R. Ramachandran, M. Vinoba, S.Y. Choi, D.H. Chu, Y. Yoon, S.C. Nam, S.K. Jeong, Facile synthesis and electrochemical properties of Co_3S_4-nitrogen-doped graphene nanocomposites for supercapacitor applications, Electroanal. 26 (2014) 199.
[37] Y. Shang, L. Cai, X. Jiang, Preparation of graphene oxide/pristine graphene/polyaniline ternary composites through a simple method and application to supercapacitor, J. Phys. Conf. Ser. 1622 (2020), 012008.
[38] T. Jiang, H. Chen, H. Wan, L. Miao, L. Zhang, Tic effect of Fe_3O_4/reduced graphene oxide nanocomposites for supercapacitors with good cycling life, Electrochim. Acta 114 (2013) 674.
[39] H. Farsi, F. Gobal, Z. Barzgari, A study of hydrated nanostructured tungsten trioxide as an electroactive material for pseudocapacitors, Ionics 19 (2013) 287.
[40] M. El-Shahat, M. Mochtar, M.M. Rashad, M.A. Mousa, Single and ternary nanocomposite electrodes of Mn_3O_4/TiO_2/rGO for supercapacitors, J. Solid State Electrochem. 25 (2021) 803.
[41] W. Wang, Q. Hao, W. Lei, X. Xia, X. Wang, Ternary nitrogen-doped graphene/nickel ferrite/polyaniline nanocomposites for high-performance supercapacitors, J. Power Sources 269 (2014) 250.
[42] B.A. Mei, O. Munteshari, J. Lau, B. Dunn, L. Pilon, Physical interpretations of nyquist plots for EDLC electrodes and devices, J. Phys. Chem. C 122 (1) (2018) 194.
[43] A.J. Bard, L.R. Faulkner, Electrochemical Methods, 2nd edn, Wiley, New Jersey, American, 2001.
[44] P.C. Gao, A.H. Lu, W.C. Li, Dual functions of activated carbon in a positive electrode for MnO_2-based hybrid supercapacitor, J. Power Source 196 (2011) 4095.
[45] J. Shasha, L. Tiehu, C. Xiong, C. Tang, A. Dang, H. Li, T. Zhao, A facile method of preparing the asymmetric supercapacitor with two electrodes assembled on a sheet of filter paper, Nanomaterials 9 (2019) 1338.
[46] M. Sun, J. Tie, G. Cheng, T. Lin, S. Peng, F. Deng, F. Ye, L. Yu, In situ growth of burl-like nickel cobalt sulfide on carbon fibers as high-performance supercapacitors, J. Mater. Chem. A 3 (2015) 1730.
[47] K.J. Huang, L. Wang, Y.J. Liu, Y.M. Liu, H.B. Wang, T. Gan, L.L. Wang, Layered MoS_2–graphene composites for supercapacitor applications with enhanced capacitive performance, Int. J. Hydrog. Energy 38 (2013) 14027.
[48] M. Sun, J. Tie, G. Cheng, T. Lin, S. Peng, F. Deng, F. Ye, L. Yu, In situ growth of burl-like nickel cobalt sulfide on carbon fibers as high-performance supercapacitors, J. Mater. Chem. A 3 (2015) 1730.
[49] M. Mousa, M. Khairy, M. Shehab, Nanostructuredferrite/graphene/polyaniline using for supercapacitor to enhance the capacitive behavior, J. Solid State Electrochem. 21 (4) (2017) 995.
[50] M. Sun, Z. Li, Q. Fang, S. Han, C. Cai, H. Li, W. Shen, X. Liuc, Y.Q. Fu, Room-temperature synthesized porous $Cu(OH)_2$/ Cu_7S_4 hybrid nanowires as a high-performance electrode material for asymmetric supercapacitors, J. Mater. Chem. A 8 (2020) 724–734.
[51] B. Bhujun, M.T.T. Tan, A.S. Shanmugam, Study of mixed ternary transition metal ferrites as potential electrodes for supercapacitor applications, Results Phys. 7 (2017) 345.
[52] S. Liu, K. Chen, C. Xue, S. Nie, J. Li, J. Zhu, Dual-ZIF-derived "reassembling strategy" to hollow MnCoS nanospheres for aqueous asymmetric supercapacitors, RSC Adv. 12 (2022) 24769–24777.
[53] C. Lamiel, Y.R. Lee, M.H. Cho, D. Tuma, J.J. Shim, Enhanced electrochemical performance of nickel-cobalt-oxide@ reduced graphene oxide//activated carbon asymmetric supercapacitors by the addition of a redox-active electrolyte, J. Colloid Interf. Sci. 507 (2017) 300–309, https://doi.org/10.1016/j.jcis.2017.08.003.
[54] R. Vinodh, R.S. Babu, R. Atchudan, H.J. Kim, M. Yi, L.M. Samyn, A.L.F. Barros, Fabrication of high-performance asymmetric supercapacitor consists of nickel oxide and activated carbon (NiO//AC), Catalysts 12 (2022) 375, https://doi.org/10.3390/catal12040375.
[55] M. Dong, Z. Wang, J. Wang, H. Guo, X. Li and G.Yan, Controlled synthesis of NixCoyS4/rGO composites for constructing high-performance asymmetric supercapacitor, Front. Mater. 6:176. doi: https://doi.org/10.3389/fmats.2019.00176.
[56] L. Mi, W. Wei, S. Huang, S. Cui, W. Zhang, H. Hou, W. Chen, A nest-like Ni@$Ni_{1.4}Co_{1.6}S_2$ electrode for flexible high-performance rolling supercapacitor device design, J. Mater. Chem. A 3 (2015) 20973–20982.